EUROPEAN ORGANIZATION FOR NUCLEAR RESEARCH
European Laboratory for Particle Physics

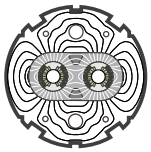

AT Beta Beam Project Note xxx

2007-01-11

Elena.Wildner@cern.ch

Large aperture superconducting dipoles for a beta beam decay ring *Provisional*

Author(s) / Div-Group: Christine Vollinger, Elena Wildner/AT-MCS

Keywords: geometry, magnet axis, saw tooth

Summary

To optimize the ratio between the straight sections and the arcs of the decay ring, proposed for the EURISOL beta beam project for neutrino production, a superconducting 6T dipole has been designed. Several options exist but this preliminary study only deals with a "cosine theta" approach. The aperture of this dipole has to be large to house the decaying ion beam and the decay products simultaneously. The dipole is protected by absorbers inside the beam-pipe. A preliminary study of the heat deposition in the coil from different absorber materials has been made.

1. Introduction

The aim of the beta beam is to produce highly energetic pure electron neutrino and anti-neutrino beams coming from β-decay of $^{18}Ne^{10+}$ and $^{6}He^{2+}$ ion beams, following the reactions

$$^{6}_{2}He^{2+} \rightarrow ^{6}_{3}Li^{3+} + e^{-} + \bar{\nu} \quad (1)$$

for Helium and

$$^{18}_{10}Ne^{10+} \rightarrow ^{18}_{9}F^{9+} + e^{+} + \nu \quad (2)$$

for Neon. In Figure 1 the Feynman diagram for the beta decay is shown.

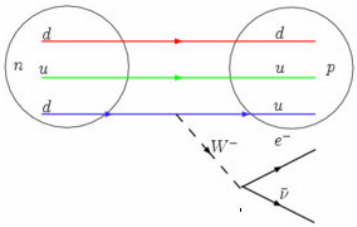

Figure 1: Feynman diagram of the beta decay.

The design of the decay ring is based on the existing CERN infrastructure [1] and the radioactive ion beams are extracted from the SPS as shown in Figure 2.

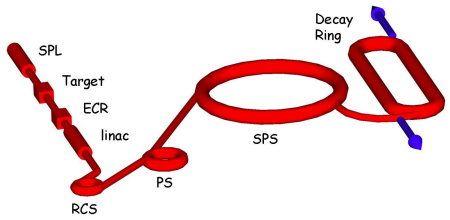

Figure 2 : Schematic view of the decay ring with injector chain.

The decay ring is a race track shaped storage ring, with a circumference of about 6900 m, the same as the CERN SPS. The about 2500 m long straight sections, where the useful decay takes place, are oriented towards the experiments in the Frejus tunnel.

The decayed ions $^{18}F^{9+}$ and $^{6}Li^{3+}$ in the machine have to be managed by introducing dumps and absorbers. These decay products have a different magnetic rigidity from the parent ion beam. Therefore, the trajectories of the child beams in the magnets are different from those of the parent ions and the child ions are lost around the machine. These problems have been addressed for the design of the decay ring lattice. This work is a first attempt to design a lattice dipole that is adapted to the beam conditions in the decay ring. We also make a first evaluation of the impact of the radioactive decay on the dipole coil. We base our calculations on a first optics design described in [2].

2. The Requirements for the Arc Dipole

The regular FODO lattice in the two arcs of the decay ring is designed to limit the aperture needed for the dipoles; the optical function β_x and the dispersion have to be small. There are ten 38.7 m long periods in each arc. At the position where the decay products would hit the lattice dipole in the arc, it is split into two independent dipoles and an absorber is inserted to intercept the decayed beams. This way, the half-cell is composed of two dipoles and two quadrupoles and the total arc length results to 994 m.

Splitting the arc dipole for particle interception is possible since the ion beams and their decay products have different magnetic rigidity. This way, the ion decay products will follow a different trajectory from the parent beam and the position where they hit the vacuum chamber is determined. In Figure 3 we show the two species decaying at the entrance of a dipole. In this figure we can see how the dipole length and aperture have been chosen to avoid that the beams impinge inside the dipole [2]. For $^{6}He^{2+}$ the choice is a

dipole length of 5.7 m for a field of 6 T. The main ion beam needs a half-aperture of 40 mm, however the dipole aperture has to be large enough to let also the decaying ions in the child beams pass. These decaying ions are intercepted after the dipoles by an absorber. The decay products of $^{18}Ne^{10+}$ have to be intercepted after the second dipole in the half-cell.

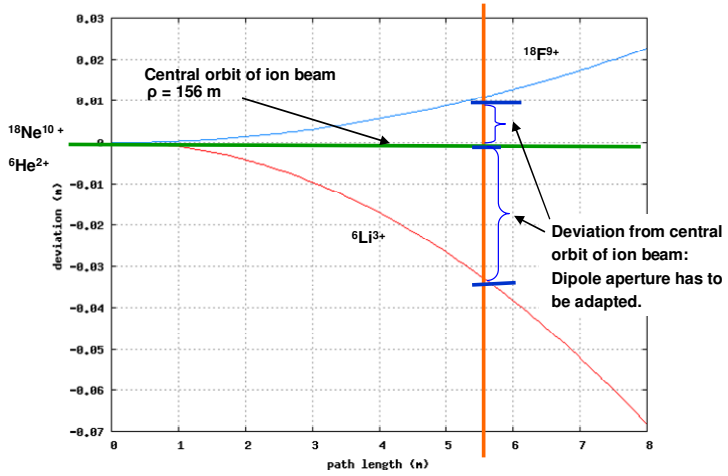

Figure 3: Decay products (child beams) and the ion beam (main beam) follow different trajectories due to different magnetic rigidity. The length and the aperture of the magnet are optimized to avoid that the particles impinge inside the dipole.

The resulting dipole parameters are shown in Table 1.

Table 1: Dipole and optics parameters for the beta beam decay ring arc.

Arc Dipole					
Bρ (Tm)	Radius (m)	Angle (rad)	Length (m)	Arc β [h],[v] (m)	Arc D (m)
1000	156	π/86	5.7	[201.2,2.6],[290.8/3.8]	10.98/-0.24

3. Design of the Main Bending Dipole

The main bending dipole magnet is a classical cos-θ design with 5 blocks in two layers and a circular aperture of 80 mm radius. The Nb-Ti cable which is used for the LHC main dipole inner layer has been chosen as a starting point due to its well-known characteristics that allowed us to omit a new cable design for this application. The layout of the magnet cross-section with the dipole field distribution is shown in Figure 4. A simple circular iron yoke with an inner radius of 132 mm is surrounding the coil (not shown). The cable [4] is made of 28 superconducting strands and has an inner and outer width of 1.736 and 2.064 mm, respectively which gives a slight keystoning. This keystoning, however, is not sufficient for a circular alignment around the mandrel which means that wedges are needed in the cross-section to achieve the required field quality.

A rather large space has been left for separating the two blocks of the outer layer which allows the insertion of a cooling pipe close to the inner layer, if needed. The required cooling will be calculated in a next step.

The multipoles are expressed in units of 10^{-4} and are calculated from the magnetic field in the aperture as $B_y(x,y)+iB_x(x,y)=\sum_{n=1}^{\infty}(B_n+iA_n)\left(\frac{x+iy}{R_{ref}}\right)^{n-1}$, where x and y are the transverse coordinates and B_n and A_n are the normal and skew multipoles calculated at a reference radius R_{ref} relative to the main field $b_n=B_n/B_1$, $a_n=A_n/B_1$. From the simulation, we have reached a main field of 6.1 T with field errors at a reference radius of 53 mm (i.e., 2/3 of the aperture radius) given in Table 2. Due to the coil symmetry in the simulation, the skew multipoles vanish.

Table 2: Calculated multipole errors in units 10^{-4} relative to the main field at a reference radius of 53 mm.

b_3	1.31	b_7	23.81
b_5	-20.10	b_9	-10.97

The cable height is 15.1 mm and its critical current at 9 T, 1.9 K exceeds 13750 A, giving a sufficiently large margin on the load line for this application (see Figure 5), allowing even a small quantity of heat load to be taken by the coil without causing a quench, if needed. For block 3 (block with highest peak field of 7.1T in the cross-section), the margin on the load line is 73.2%. The goal, however, is to intercept all particles by the absorbers after each dipole.

The coil end has been designed in dimensions as compact as possible in order to leave sufficient space needed for the absorbers with a maximum peak field in the coil end of 6.3 T.

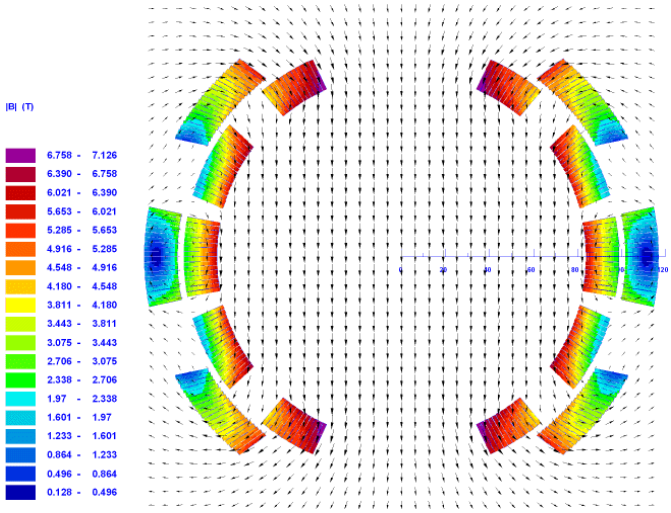

Figure 4: Cross-section of the main bending dipole with an 80-mm aperture with main field lines and peak field distribution in the coil.

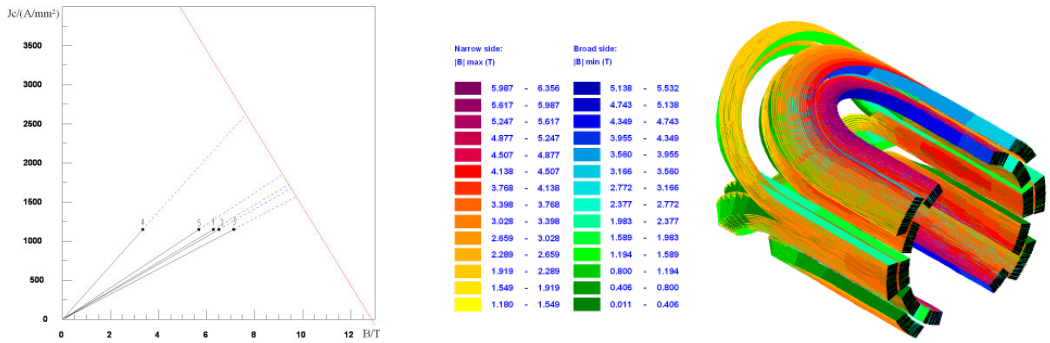

Figure 5: Left: Margin on the load-line Jc versus B for inner layer blocks (no. 1-3) and outer layer blocks (no. 4-5). Right: View of the non-connection side coil end of the dipole with corresponding peak field distribution.

4. Forces in the Dipole Cross-section

We carried out an estimation of the force distribution in the cross-section of the arc dipole to determine the stress on the coil midplane by calculating the azimuthal force in each conductor. Figure 6 shows the resulting force vector on each block. It can be seen from the plot that the forces concentrate on three blocks and that the inner layer is pressing against the outer in the high field regions whereas in the outer layer only an azimuthal force occurs. The stress on the midplane adds up to 15.7 MPa and 11.3 MPa in the inner and outer layer, respectively. These numbers correspond to 1.04 MN/m in the inner layer and 0.7 MN/m and are within the accepted values for this cable (for comparison, in the LHC this cable is subjected to a horizontal force component at nominal field of 1.8 MN/m [4]).

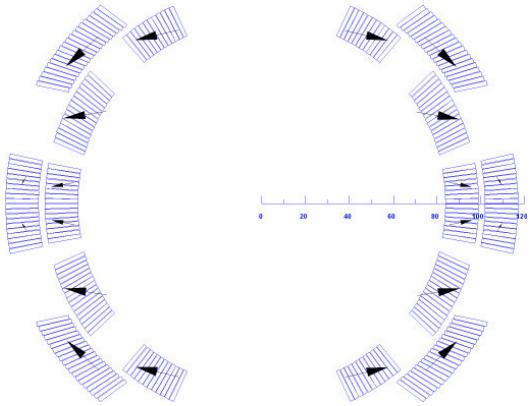

Figure 6: Force distribution in the coil cross-section. Arrows show the resulting force in for each block.

5. Heat Deposition in Dipole Coil

For the stored beams in the decay ring, the lost power is around 10 W/m. Absorbers have been inserted, after each dipole, to intercept the loss. In Figure 7 we see the projection on a plane perpendicular to the ion beam direction. The decay products for the two species are absorbed but the aperture is large enough for the circulating ion beam.

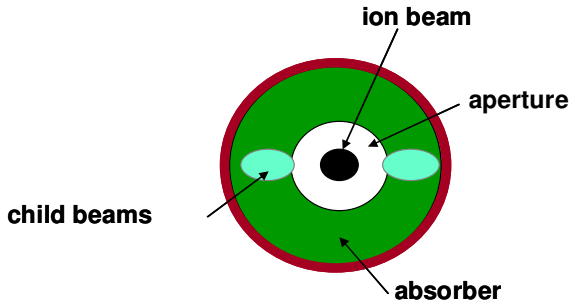

Figure 7: Transverse projection of the beams, the absorber and the aperture for the ion beam.

In Figure 8 we see the dipoles, the two decayed beams and the absorbers.

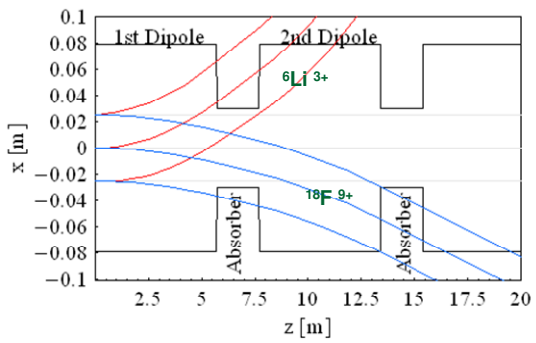

Figure 8: The arc lattice half cell: Absorbers have been inserted between the dipoles to intercept the decay products $^{6}Li^{3+}$ and $^{18}F^{9+}$.

The heat deposition model only takes into account absorbers inside the stainless steel beam pipe and further studies may include dimensioning and radiation studies of absorbers outside the chamber, inserted between the magnets to protect the coil ends. Absorber material should be non-magnetic so, for example, iron and lead should be avoided. The optics has been designed such that the major part of the decay products impinges on the absorbers. In the straight sections, the decay products are not bent by the dipole field and they follow the ion beam. When entering the dipole, all decayed ions accumulated in the straight sections form a concentrated beam. This beam will be absorbed by the absorbers. It can be understood from Figure 8 that, in the second half of the second dipole, some of the continuous loss in the first dipole will not be absorbed. The absorbers between the magnets absorb the peaks of the decay products and the resulting heat deposition in the coils has been estimated to see if the absorber is efficient and has a good design. The peak losses (see Figure 9) have been simulated by including in the model all particles, decaying in the straight section up to the next dipole (1.4 10^{9} particles/s). Care has been taken to check that, for this simple model, heat from the simulated beam is not deposited in the second half of the dipole (we would like to avoid accumulated loss from the simulated beam and from the continuously decaying beam in the dipoles).

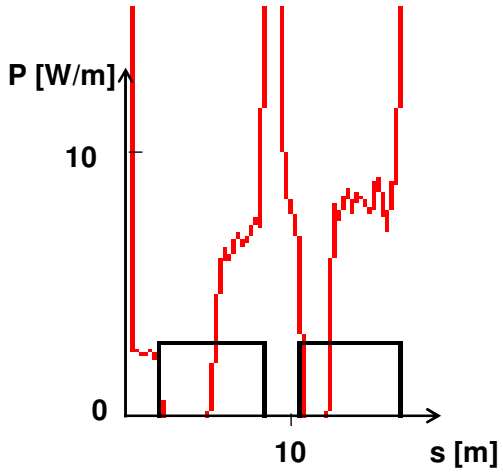

Figure 9: The peak energy deposition happens between the dipoles (by design). Some of the particles decay in the dipole and impinge on the walls in the second half of the next magnet (around 1 W/m). s is the longitudinal coordinate of the machine.

The particles taken into account in the model have been considered, for this first estimation, as a pencil beam of $^{6}Li^{3+}$ with the same momentum, 94 GeV/nucleon, as the ion beam. The modelling was made using protons and not the ion (only a matter of simplification for a more detailed study we will put the ions in the model). This beam is bent in the dipole and impinges on the absorber in the beam pipe. The model is shown Figure 10. Further refined studies have to take into account all decayed particles along the machine by detailed tracking. In the heat deposition model the coils are modelled as a hollow cylinder inside the yoke, also a cylinder. The beam-pipe and the insulation between the pipe and the coil are implemented.

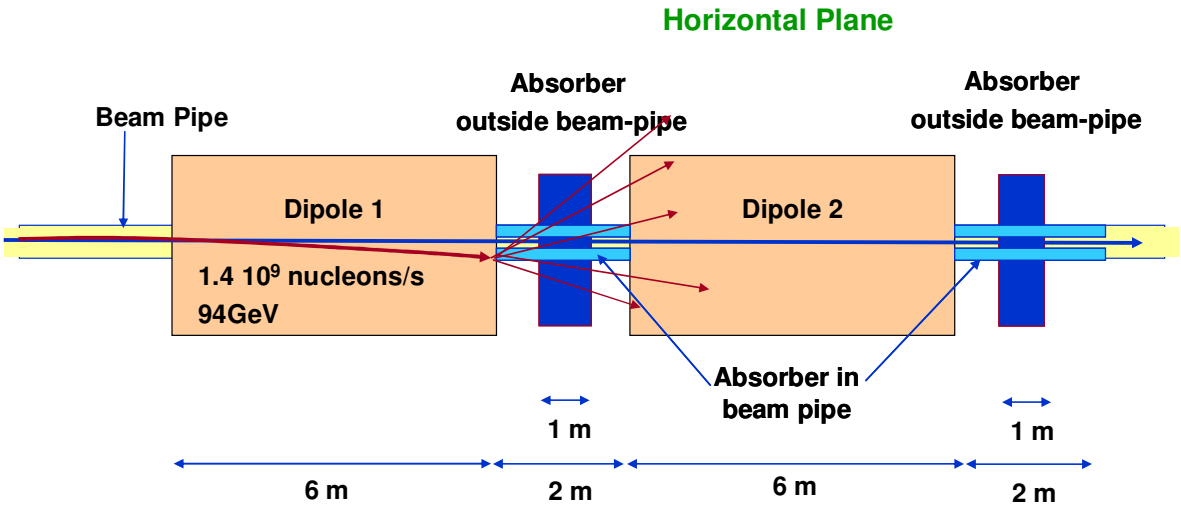

Figure 10: Model for heat deposition calculation in the large aperture dipole coil.

We used the FLUKA [1] code for the calculations. The geometry was generated using Simplegeo [3] and the resulting model can be seen in Figure 11.

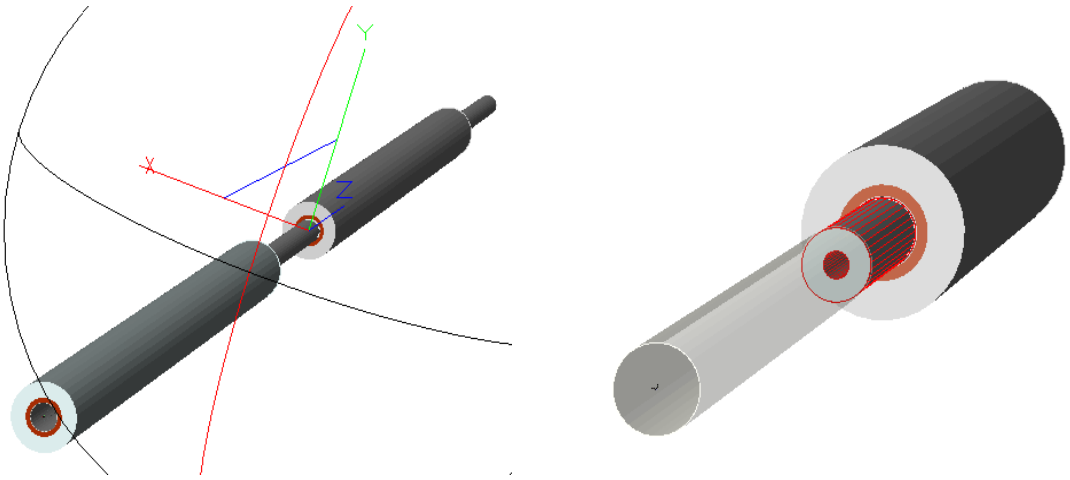

Figure 11: The geometry modelled in Simplegeo, to the left the complete model and to the right we have taken out the first dipole to show the absorber in the beam pipe, highlighted in red.

We have checked the heat deposition using carbon, stainless steel and tungsten and also checked the case without absorber. Heat deposition has only been scored in the dipole coil, in cells with sizes corresponding to the transverse dimension of each cable (15 mm radial and 1.5 mm azimuthal width and with a length of 20 mm). This corresponds to local heat deposition in steady state operation. The results are shown in table 3, where the values in the cell with the highest heat deposition in the magnet coil are shown. The distance from the dipole entrance and the angular position of the maximum is also shown. Statistical variations in the calculations are estimated to less that 0.5 mW and for stainless steel and tungsten the values found were below 0.5 mW.

Table 3: Maximum deposited heat in the coil for different absorber materials.

Absorber Material/Quantity	Max Heat (mW/cm3)	Distance form dipole entrance (cm)	Azimuthal angle for max (degrees)
Vacuum	>30	~200	~0
Carbon	1.4	20	7
Stainless Steel	<0.5	-	-
Tungsten	<0.5	-	-

The distribution of the deposited energy for carbon can be seen in Figure 12. In the figure we show the heat deposition around the magnet at the distance from the entry where we find the highest heat deposition. For comparison, for the LHC magnet energy deposition quench threashould in the coil is 4.3 mW/cm^3. The maximum we found lies in the mid plane.

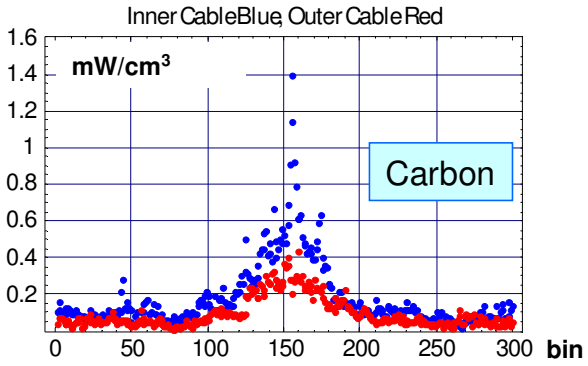

Figure 12: Results for heat deposition using a carbon absorber. The20 mm long slice shown is the one that has the maximum heat deposition. It is situated at 20 cm from the entrance of the dipole. The 300 bins cover 2π rad. The mid plane corresponds to the 150th bin.

Interesting is also to see where the energy is deposited along the magnet. To be conservative, the energy from the pencil beam of accumulated particles should be deposited in the first half of the magnet. In the second half we have energy deposition also from the beams decaying inside the dipole. For this first, simplified estimation we want to make sure that the essential part of the deposited energy falls in the first half, see Figure 13. In the figure the green line in the middle of the dipoles corresponds to the middle of the dipole and is shown to make sure that the heat spot is in the first half so that we do not accumulate heat deposition from the continuously decaying beams in the dipoles.

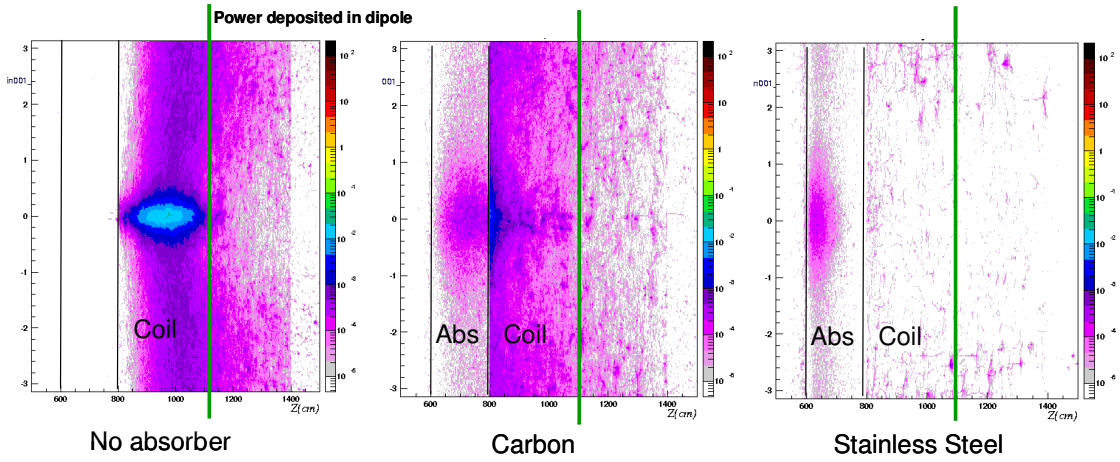

Figure 13: The heat deposition from the modelled beam falls essentially in the first half of the dipole which is important to make sure we have limited overlap with the decayed beam created inside the dipole. The scale is the same for all cases but has no meaning for absolute values.

:

6. Future work and Conclusion

A preliminary design of a superconducting large aperture dipole magnet for the beta beam decay ring has margins for multipoles and load line. The heat deposition is low enough not to quench the magnet in steady state operation conditions if we use carbon absorbers between the magnets. This choice gives us a margin of a factor 3 which has to be carefully checked with refined simulations. Stainless steel would have very good margins. The influence of absorbers on beam stability has to be evaluated by impedance studies. A

first estimation [5] shows that the structure as it is described here would create too large impedances. However, with a "beam screen" covering a large enough area, leaving an opening for the decaying beams, could be enough to keep the impedances within required limits. See Figure 14.

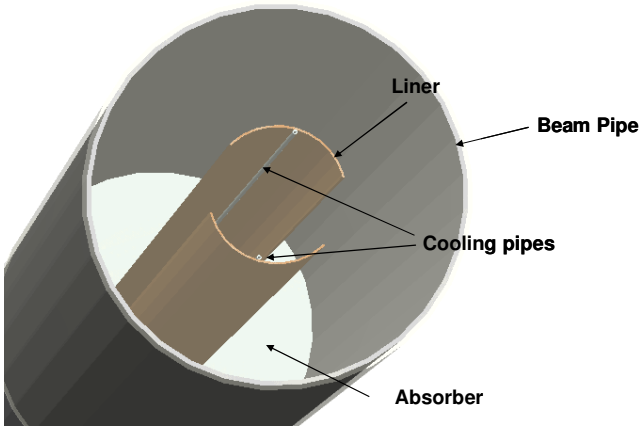

Figure 14: To reduce impedances a liner can be installed above and below the beam inside the absorbers. A cooling pipe in the "beam screen" to cool the absorbers can be envisaged.

Another solution would be an open mid-plane dipole. Here also we have to make sure that particles impinging on the beam pipe do not deposit energy in the coils. Detailed tracking of the decay products have to be made using code especially developed for this (ACCIM [6]) and a refined heat deposition model has to be developed. Cryogenics and irradiation aspects have to be further investigated.

References

[1] A. Fasso`, A. Ferrari, J. Ranft, and P.R. Sala, "FLUKA: a multi-particle transport code", CERN-2005-10 (2005), INFN/TC_05/11, SLAC-R-773

[2] A. Chancé, J. Payet, "First design for the optics of the decay ring for the beta-beams", April 2006, EURISOL report DS/TASK12/TN-06-05

[3] Theis C., et al., "Interactive three dimensional visualization and creation of geometries for Monte Carlo calculations", Nuclear Instruments and Methods in Physics Research A 562, pp. 827-829 (2006).

[4] LHC Design Report, Vol. 1, page 157, ISBN 92-9083-224-0

[5] Erk Jensen, CERN, private communication

[6] F.W. Jones , TRIUMF, "Development of the ACCSIM tracking and simulation code", PAC 1997